Journal of Geophysical Research: Planets

RESEARCH ARTICLE
10.1029/2018JE005765

Controls on the Formation of Lunar Multiring Basins

Brandon C. Johnson[1], Jeffrey C. Andrews-Hanna[2], Gareth S. Collins[3], Andrew M. Freed[4], H. J. Melosh[4], and Maria T. Zuber[5]

[1]Department of Earth, Environmental and Planetary Sciences, Brown University, Providence, RI, USA, [2]Department of Planetary Science, Lunar and Planetary Laboratory, University of Arizona, Tucson, AZ, USA, [3]Impacts and Astromaterials Research Centre, Department Earth Science and Engineering, Imperial College London, London, UK, [4]Department of Earth, Atmospheric, and Planetary Sciences, Purdue University, West Lafayette, IN, USA, [5]Department of Earth, Atmospheric and Planetary Sciences, Massachusetts Institute of Technology, Cambridge, MA, USA

Abstract Multiring basins dominate the crustal structure, tectonics, and stratigraphy of the Moon. Understanding how these basins form is crucial for understanding the evolution of ancient planetary crusts. To understand how preimpact thermal structure and crustal thickness affect the formation of multiring basins, we simulate the formation of lunar basins and their rings under a range of target and impactor conditions. We find that ring locations, spacing, and offsets are sensitive to lunar thermal gradient (strength of the lithosphere), temperature of the deep lunar mantle (strength of the asthenosphere), and preimpact crustal thickness. We also explore the effect of impactor size on the formation of basin rings and reproduce the observed transition from peak-ring basins to multiring basins and reproduced many observed aspects of ring spacing and location. Our results are in broad agreement with the ring tectonic theory for the formation of basin rings and also suggest that ring tectonic theory applies to the rim scarp of smaller peak-ring basins.

Plain Language Summary The largest impact craters on the Moon are multiring basins that exhibit three or more topographic rings. Great volumes of material were ejected and redistributed during the formation of these 1,000-km-scale basins. Formation of these basins is the predominant process driving change of the lunar crust, the outermost layer of the Moon. Why large basins have multiple topographic rings and what they might tell us about the Moon remain poorly understood. Here we simulate the formation of these basins and their rings during an asteroid impact. We explore how thickness of the lunar crust, size of the impacting body, and interior temperature of the Moon affect the formation of basins and their rings. With well-persevered multiring basins and an abundance of high-quality gravity and topography data, the Moon is an ideal location to explore the formation of multiring basins. A better understanding of the formation of these basins will help us understand how similar basins may have affected the crusts of the Earth, Mars, Mercury, and Venus.

Key Points:
- We simulate the formation of multiring basins exploring the effect of impactor size, target thermal structure, and crustal thickness
- Our simulations reproduce observed trends in ring spacing including the transition from peak-ring to multiring structures
- Our results show that basin ring formation is quite sensitive to target thermal structure in general agreement with ring tectonic theory

Correspondence to:
B. C. Johnson,
brandon_johnson@brown.edu

Citation:
Johnson, B. C., Andrews-Hanna, J. C., Collins, G. S., Freed, A. M., Melosh, H. J., & Zuber, M. T. (2018). Controls on the formation of lunar multiring basins. *Journal of Geophysical Research: Planets*, *123*, 3035–3050. https://doi.org/10.1029/2018JE005765

Received 24 JUL 2018
Accepted 26 OCT 2018
Accepted article online 5 NOV 2018
Published online 21 NOV 2018

1. Introduction

Impact cratering is a ubiquitous and important process in the evolution of ancient planetary crusts. Early in the cratering process a shockwave propagates through the target, followed by a rarefaction or release wave. After propagation of the shock and rarefaction, the underlying material is left with a residual velocity that sets up the excavation flow, opening up a bowl-shaped transient crater (Melosh, 1985). For small craters, of less than about 15-km diameter on the Moon, material from the steep crater rim collapses into the open cavity, partially filling it with a breccia lens (Collins, 2014; Dence, 1965). This ultimately produces a bowl-shaped simple crater. When the final lunar crater is larger than ~15 km in diameter, the transient crater collapses wholesale producing a complex crater with an uplifted floor, central peak, and terraced crater walls (Melosh & Ivanov, 1999). On the Moon, when the final crater diameter exceeds ~200 km (Baker et al., 2011), the central uplift is unstable and collapses downward and outward producing a concentric peak ring (Kring et al., 2016; Morgan et al., 2016). Above ~600 km in diameter, multiring basins that exhibit three or more concentric topographic rings are produced on the Moon (Neumann et al., 2015). Although the process of impact cratering is reasonably well understood (Melosh, 1989), the formation of multiring basins is a complicated multistage process, which is ripe for further study.

Other than the 2,000-km-scale elliptical South Pole-Aitken basin (Garrick-Bethell & Zuber, 2009), which may be a multiring basin itself (Hiesinger & Head, 2004), multiring basins are the largest impact structures on

Table 1
iSALE Model Setup

Description	Value
Size of high-resolution cell	1 km
Number of high-resolution cells, horizontal direction	500
Number of high-resolution cells, vertical direction	700
Physical dimension of entire mesh, horizontal direction	0 to 1,796 km
Physical dimension of entire mesh, vertical direction	−3,695 to 387 km
Impact velocity	15 km/s
Surface gravitational acceleration	1.59 m/s^2
Target radius	1,740 km
Core radius	350 km
Surface temperature	300 K

the Moon (Neumann et al., 2015). Multiring basins dominate the stratigraphy, tectonics, and crustal structure of the Moon at scales of hundreds to thousands of kilometers (Spudis et al., 1994; Wieczorek et al., 2013; Wilhelms, 1987; Zuber et al., 2016). Understanding how these large basins formed is paramount to understanding the early evolution of planetary crusts.

Recent work on the formation of multiring basins has focused on Orientale, the freshest multiring basin on the Moon. Orientale has three well-defined topographic rings. Orientale's outer two rings, the Outer Rook and Cordillera, located at $R \approx 310$ and 460 km (Andrews-Hanna et al., 2018), respectively, appear to be large fault scarps (Nahm et al., 2013). High-resolution gravity data from Gravity Recovery and Interior Laboratory reveal that the Outer Rook and Cordillera have locally thinned the crust and offset the crust-mantle interface (Andrews-Hanna et al., 2018; Zuber et al., 2016). Both of these characteristics are consistent with normal faults cutting through the crust-mantle interface (Andrews-Hanna et al., 2018; Zuber et al., 2016). The topography of Orientale's innermost ring, the Inner Rook located at $R \approx 230$ km, indicates that it is related to the peak rings of smaller basins (Andrews-Hanna et al., 2018; Nahm et al., 2013).

Basin formation models of Potter et al. (2013) and Potter (2015) demonstrated subtle strain localization suggestive of ring fault formation during crater collapse. Building on this work, Johnson et al. (2016) produced simulations of the Orientale forming impact that clearly resolved the development of basin rings with kilometer-scale fault offsets. In addition to forming rings in approximately the correct locations, models with preimpact crustal thicknesses that range from 48 to 52 km produced excellent fits to the azimuthally averaged crustal thickness profile of Orientale derived from GRAIL gravity and Lunar Orbiter Laser Altimeter topography (Johnson et al., 2016). In these simulations the Inner Rook forms by collapse of a central uplift similar to the dynamic collapse model for the formation of peak rings (Kring et al., 2016; Morgan et al., 2016). Johnson et al. (2016) found that the Outer Rook and Cordillera, the outer rings of Orientale, are large normal faults that form during crater collapse. These faults offset the crust-mantle interface and locally thin the crust consistent with constraints from GRAIL gravity (Andrews-Hanna et al., 2018; Zuber et al., 2016). In

Table 2
iSALE Material Input Parameters

Description	Value for crust	Value for mantle	References
Equation of state	ANEOS granite	ANEOS dunite	d, e
Melting temperature[a]	1,513 K	1,373 K	f, g
Thermal softening parameter[a]	1.2	1.1	f, g
Simon A parameter[b]	1,840 MPa	1,520 MPa	f, g
Simon C parameter[b]	7.27	4.05	f, g
Poisson's ratio	0.25	0.25	f, g
Frictional coefficient (damaged)[a]	0.71	0.63	f, g
Frictional coefficient (undamaged)[a]	1.1	1.58	f, g
Strength at infinite pressure[a]	2.49 GPa	3.26 GPa	f, g
Cohesion (damaged)[a]	0.01 MPa	0.01 MPa	f, g
Cohesion (undamaged)[a]	31.9 MPa	5.07 MPa	f, g
Brittle ductile transition[a]	1.23 GPa	1.23 GPa	a
Brittle plastic transition[a]	2.35 GPa	2.35 GPa	c
Initial tensile strength[a]	10 MPa	10 MPa	c
Maximum distension[c]	1.2	1.2	c
Maximum dilatancy coefficient[c]	0.045	0.045	c
Dilatancy pressure limit[c]	200 MPa	200 MPa	c
Frictional coefficient (maximum distension)[c]	0.4	0.4	c

[a]Parameters for a rock like material strength model (Collins et al., 2004). [b]Parameter that describes a material's pressure-dependent melt temperature (Wünnemann et al., 2008). [c]Parameters for iSALE's dilatancy model implemented and described by Collins (2014). [d]Benz et al. (1989). [e]Pierazzo et al. (1997). [f]Davison et al. (2010). [g]Potter et al. (2012).

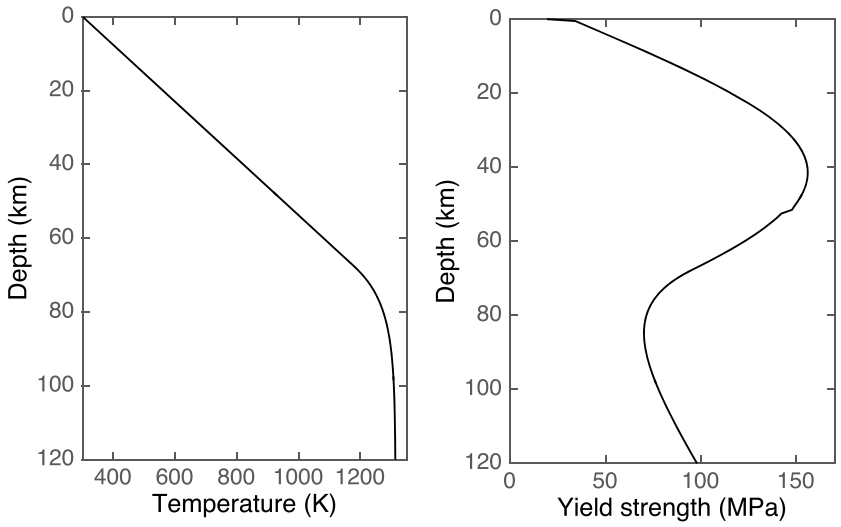

Figure 1. (left) Preimpact temperature and (right) material strength as a function of depth in the target for our fiducial model. This represents a 13-K/km thermal gradient from a surface temperature of 300 K. The model has crustal thickness of 52 km.

the simulations of Johnson et al. (2016) faults formed as the result of inward flow of warm and weak mantle material during collapse of the transient cavity. This flow of weaker underlying material pulls the cooler crust along with it, ultimately causing extensional faulting with large offsets far from the transient cavity rim. The importance of the weak underlying mantle material is consistent with ring tectonic theory of multiring basin formation (Melosh & McKinnon, 1978).

The simulations of Johnson et al. (2016) were focused on reproducing the GRAIL- and LOLA-derived crustal structure of Orientale and the location and spacing of Orientale rings. Thus, their exploration of parameter space was rather limited. To elucidate the parameters important to multiring basin formation, we expand the parameter space to conditions representative of the formation of nearly all lunar basins. In section 2 we describe our methodology. In section 3.1 we describe our fiducial simulation, which we use for comparison to assess the role of various parameters. In section 3.2 we explore the role of impactor size and the transition from peak-ring to multiring basins. In sections 3.3 and 3.4 we investigate the importance of target thermal structure. In section 3.5 we study the effects of target crustal thickness. In section 4 we discuss the implications of our results.

2. Methods

Following Johnson et al. (2016), we simulate basin formation using iSALE, a multimaterial, multirheology, finite difference, shock physics code (Amsden et al., 1980; Collins et al., 2004; Wünnemann et al., 2006). As a continuum model, iSALE cannot resolve discontinuous slip planes; instead, faults are regions of concentrated strain. As in Johnson et al. (2016), we include several improvements over previous models (Freed et al., 2014; Ivanov et al., 2010; Miljkovic et al., 2013; Potter, 2015; Potter et al., 2013) that allow us to simulate the formation faults with kilometers-scale offsets. We include the dilatancy model of Collins (2014). In addition to accounting for porosity increases associated with the deformation of rocks, dilatancy can also cause or enhance strain localization (Montési, 2002). We use a damage model where the transition from intact to fractured rock strength is an exponential function of plastic strain. Johnson et al. (2016) found that this damage model results in more localization at large strains compared with simpler damage models where the transition from intact to fractured rock strength is a more abrupt linear function of plastic strain (Montési, 2002). For large basins, like Orientale, the curvature of the target surface is influential. Thus, we simulate impacts onto a spherical target in a central gravity field.

In this work we include two more improvements from the models of Johnson et al. (2016). We include a stress dependent viscoelastic-plastic rheology for mantle material, which was recently added to iSALE (Elbeshausen

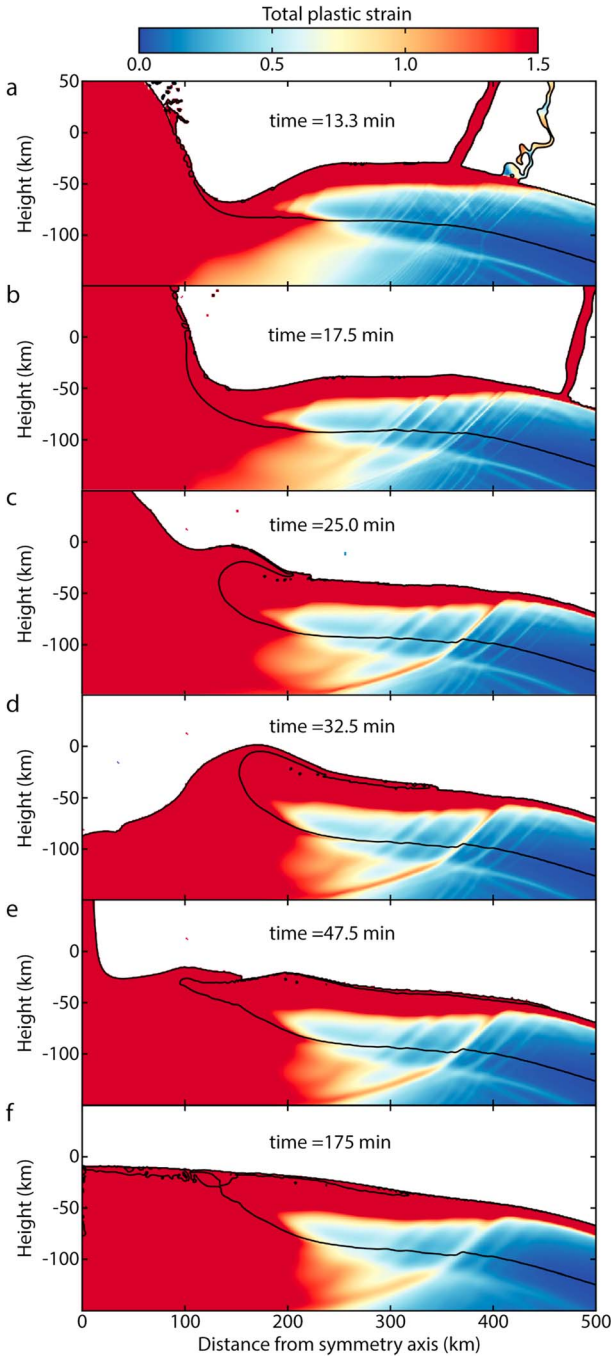

Figure 2. Time series showing crater collapse and ring formation in our fiducial model (dT/dz = 13 K/km, t_{crust} = 52 km, D_{imp} = 64 km, V_{imp} = 15 km/s). Material is colored according to total plastic strain as indicated by the scale bar. Initial impact occurs at the origin. The thin black curves are the boundary or interface between two materials including, crust, mantle, and void.

& Melosh, 2018). We also include tensile failure, which is neglected by default to reduce computational expense. Although all other setup parameters are the same as those used by Johnson et al. (2016), for completeness, we include here a tabular description of the iSALE model setup (Table 1) and material input parameters (Table 2).

Our fiducial simulation is of a 64-km-diameter dunite impactor striking a Moon-like target at 15 km/s (Le Feuvre & Wieczorek, 2011; Yue et al., 2013). The target has a 52-km-thick crust, a surface temperature of 300 K, and a near-surface thermal gradient of 13 K/km. The ANEOS equation of state for granite (Pierazzo et al., 1997) is used to represent the crust because it is the most suitable analog in terms of density among the limited number of equations of state that can accurately model the behavior of geologic materials shocked to high temperature and pressure. Below the lithosphere, we assume an adiabatic thermal profile (~0.045 K/km) appropriate for convecting material at ~1,300 K (Figure 1). The results of this simulation are described in detail in section 3.1. To explore the effects of impactor size (section 3.2) and crustal thickness (section 3.3), we vary impactor diameter from 40 to 70 km and preimpact crustal thickness from 20 to 60 km. The exploration of impactor size is the simplest way to examine differences between basins of different sizes, with all other parameters being equal. As will be seen in the results, the chosen range of impactor size results in basins spanning the transition from peak-ring to multiring basins. The chosen range of crustal thickness values encompasses both typical nearside and typical farside crustal thicknesses (Wieczorek et al., 2013).

We explore the effect of target thermal structure by varying lunar thermal gradient from 10 to 25 K/km (section 3.4) For comparison, one thermochemical evolution model, which assumes a crustal thermal conductivity of 1.5 W/m/K, predicted that temperature gradients are 36–39 K/km within the nearside Procellarum KREEP Terrane (PKT) and 12–16 K/km over the farside from 3.5 to 4 Ga (Laneuville et al., 2013). Models of current-day heat flow in agreement with Apollo measurements imply thermal gradients of 6–18 K/km depending on distance from the PKT (Laneuville et al., 2013). In this work, when material exceeds its pressure-dependent melt temperature, it is treated as a strengthless fluid. Thus, to avoid strengthless material preimpact, we vary the temperature of warm mantle over a limited range from 1,200 to 1,400 K (section 3.5). Our largest transient craters reach a depth of ~200 km, and our models are likely relatively insensitive to material strength beyond this depth. Thermal models indicate that at 3.5–4 Ga much of the shallow mantle under the PKT is at or above the solidus (~1,500 K at 200-km depth), while on the farside at 200-km depth the mantle may have a temperature of 1,100 K (Laneuville et al., 2013; Miljkovic et al., 2016). Neglecting the South Pole Aitken basin, a full exploration of this parameter space would encompass a representative range of lunar basin formation conditions (Miljkovic et al., 2013; Wieczorek et al., 2013). Our limited exploration of this parameter space and comparison to our fiducial model will provide insight into the important controls on the formation of lunar multiring basins.

3. Results

3.1. Fiducial Simulation

We first describe the formation of various ring structures in our fiducial model. Figure 2 shows a time series of the formation of a basin similar in scale to Orientale as the result of our fiducial simulation. In Figure 2, and

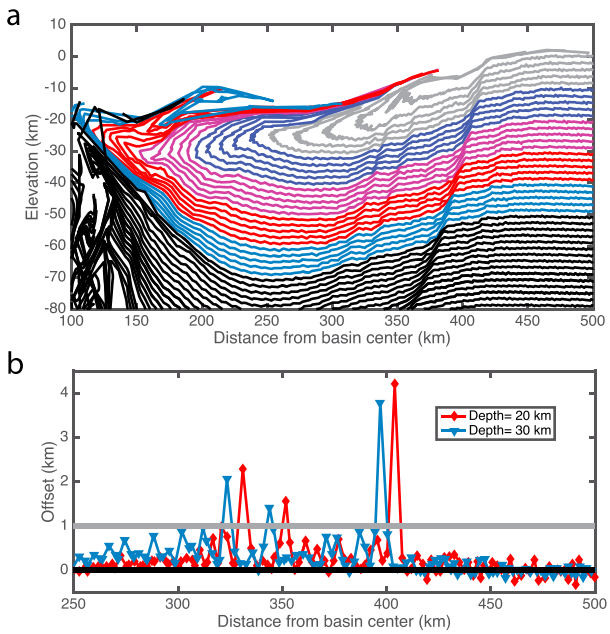

Figure 3. Fault locations and offsets from our fiducial model. Note that horizontal axis begins at 100 km in frame a and 250 km in frame b. (a) Lines connecting tracer particles that were initially at equal depths are plotted. Elevation and distance from basin center are calculated with respect to a sphere. On this type of plot, before impact the tracer lines are parallel horizontal lines with a constant spacing. In the crust lines change color every 10 km in preimpact depth and mantle material is colored black. Note that when tracers are orphaned from their nearest neighbor, the line connecting them may cross over other materials (this is seen where mantle material has been emplaced on top of crust ~120 km from the basin center). (b) Offset calculated as the change in distance between tracers originally at a constant depth of 20 (red) and 30 km (blue). Offsets are plotted midway between the displaced tracers. The thick gray line in (b) acts as a guide to the eye marking 1-km displacement. All frames are plotted 50 min after impact.

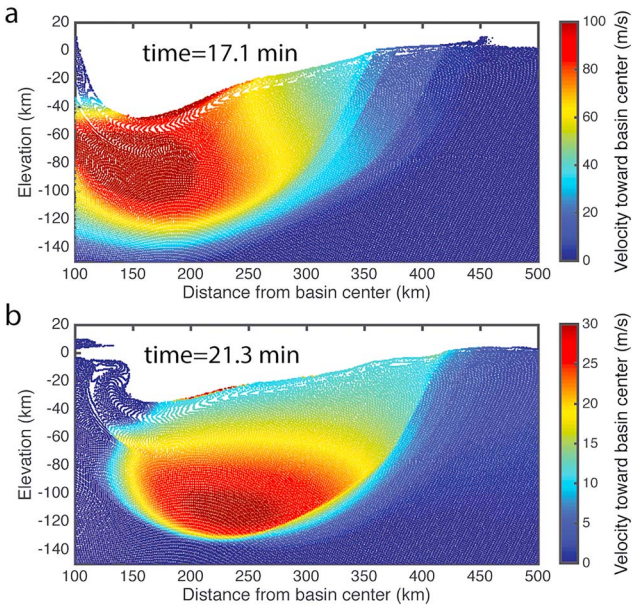

Figure 4. Material velocity showing formation of ring faults with large offsets. Tracer particles are colored according to their velocity toward the basin center. Elevation, distance from basin center, and velocity toward basin center are calculated with respect to a sphere (distance from basin center is $r\theta$, in a spherical coordinate system referenced to the center of the Moon). Note that the color scale changes between frames.

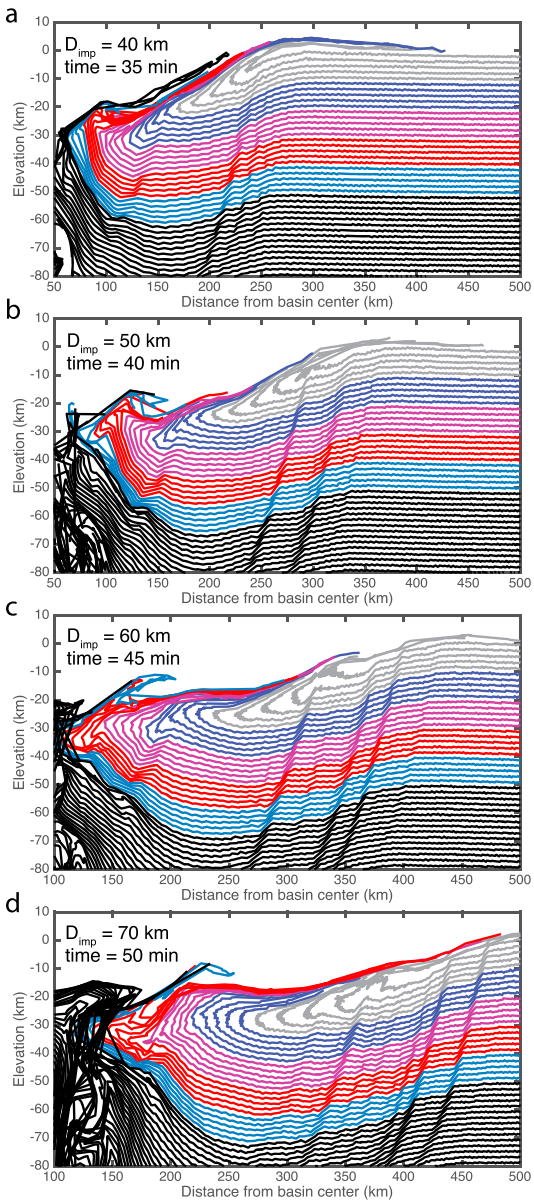

Figure 5. Vertically exaggerated plot demonstrating how impactor size affects ring spacing and location. For more information about these plots see Figure 3. Note that the horizontal axis starts at 50 km for frames a and b but begins at 100 km for frames c and d. Other than impactor size, as indicated, all other parameters are the same as in the fiducial model.

Table 3
Location of Ring Structures on Simulated Basin Showing Effect of Impactor Size

Impactor diameter (km)	Peak ring diameter (km)	Inner ring fault diameter (km)	Outer ring fault diameter (km)
40	200	NA	500
50	250	600	695
60	370	665	800
70	450	755	950

throughout this work, we interpret areas of localized high total plastic strain, $\varepsilon_{plastic}$, as candidate locations for fault zones. For brevity, we will refer to these as *faults* acknowledging that even at the unprecedented spatial resolution of our simulations, the widths of individual faults are unresolved even when resolvable fault displacements are recorded. As we step through this simulation and focus on formation of various ring structures, we will also reference Figure 3. Figure 3a is a vertically exaggerated plot where ring faults appear as offsets in tracer lines—lines connecting Lagrangian tracer particles that were originally arranged at a constant depth from the Moon's surface. Figure 3b more directly measures the offset associated with ring faults.

The impact first produces a bowl-shaped transient crater, which collapses producing the large central uplift apparent at 13.3 min (Figure 2a). At this time, ejecta are emplaced on the crust where the outer rings will eventually form (Figure 2a). With a linear scale for $\varepsilon_{plastic}$, dozens of small-scale faults with $\varepsilon_{plastic} \approx 0.5$ are already apparent (Figure 2a). Some of these faults dip away from the basin center, while others dip toward the basin center. At 17.5 min after impact (Figure 2b), continued inward flow of material has increased the scale and height of the central uplift and three to four of the small-scale faults apparent at earlier times now have much higher $\varepsilon_{plastic}$. There are two faults that come to the surface near 350 km from the basin center that produce the surface expression of what we interpret to be the basin's inner fault ring (Figures 2b and 3). This ring is analogous to Orientale's Outer Rook Ring. If the strain from these two faults was accommodated on a single fault, it would have an offset of ~4 km. At 25 min after impact (Figure 2c), the central uplift has begun collapsing, but farther from the basin center (~420-km radius) continued inward flow of material has produced an outer ring fault with >4 km of offset (Figure 3). This ring is analogous to Orientale's Cordillera Ring. After this time, modification of the ring faults is minimal. The ratio of the location of the outer ring to the location of the inner ring is 1.2 in this simulation. This spacing is substantially smaller than the often cited $\sqrt{2}\approx1.41$ spacing (Melosh, 1989). We discuss this discrepancy in ring spacing in more detail in sections 3.2 and 4.

Ring tectonic theory suggests that ring faults result from inward asthenospheric flow during crater collapse (McKinnon & Melosh, 1980; Melosh & McKinnon, 1978). This flow exerts a drag force on the base of the lithosphere causing the lithosphere to fail in extension. This failure produces large-scale circumferential normal faults and downdropped, rotated annular lithospheric blocks (McKinnon & Melosh, 1980). In Figure 2, $\varepsilon_{plastic}$ is enhanced at depths greater than ~80 km where material is relatively weak (Figure 1). The dynamics of this flow and the formation of ring faults are more easily seen in Figure 4, which demonstrates that the simulated faults have broken the lithosphere into annular blocks that move relatively independently from the rest of the lithosphere. The inward velocity increases with depth moving along the fault. This velocity structure is indicative of rotation of these lithospheric blocks. Thus, the formation of faults in our simulation is broadly consistent with the ring tectonic theory of multiring basin formation (McKinnon & Melosh, 1980; Melosh & McKinnon, 1978).

By 32.5 min (Figure 2d) collapse of the central uplift has pushed material outward, producing a bulge of uplifted material ~180 km from the basin center. This bulge is unstable and collapses back in toward the basin

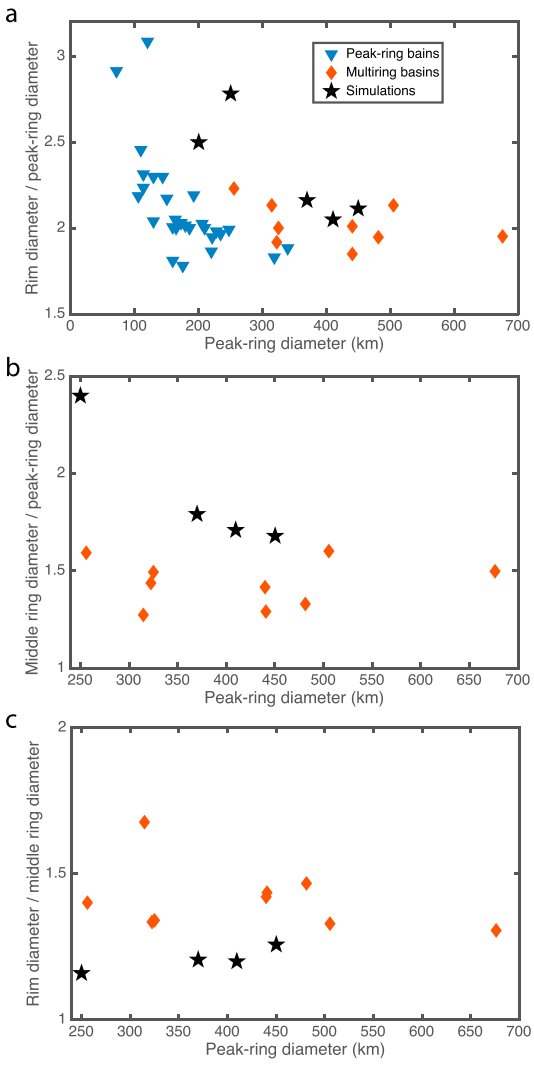

Figure 6. Comparison of simulation results to observed ring location and spacing. Note that frames b and c only include multiring basins and the horizontal axes begin at 240 km. The ring locations come from Neumann et al. (2015) and include all peak-ring and multiring basins that have reported ring locations (i.e., not an estimate of expected ring location based on scaling). The middle ring refers to the inner ring fault in our models, and the rim corresponds to the outer ring fault.

center (Figure 2e). Similar crustal deformations were observed in earlier Orientale impact simulations that neglected the curvature of the Moon (Potter et al., 2013). This process produces a topographic ring ~205 km from the basin center (Figure 3a). This ring is analogous to Orientale's Inner Rook Ring. This ring is not a ring fault and is more similar to the peak rings of smaller basins (Nahm et al., 2013). During collapse of the central uplift mantle material flows out over the basin floor (Figures 2d and 2e). As discussed by Johnson et al. (2016), this mantle flow may only occur because the height of the central uplift is exaggerated in our axisymmetric simulations. Approximately 3 hr after the impact (Figure 2f), crustal material has migrated all the way to basin center and large-scale motion has ceased.

Although there are many faults apparent in Figure 2, the faults that show up most clearly in Figure 3a have offsets exceeding 1 km (Figure 3b). These faults with kilometer-scale offsets are most consistent with the rings of multiring basins (Andrews-Hanna et al., 2018; Nahm et al., 2013). If smaller-scale ring faults are present in multiring basins, they have likely been obscured by subsequent bombardment or the basin's own ejecta in the case they form before ejecta emplacement (e.g., Figure 2a). Future detailed seismic profiles could help determine if small-scale ring faults are produced. We will, in general, focus on faults with kilometer-scale offsets and use plots such as Figure 3a to compare ring structures of basins produced under different impactor and target conditions. Because we will not discuss temporal aspects of ring formation for all simulations, we briefly summarize aspects of the fiducial model that are general to all our simulations. In all our simulations, faults with large offsets form after emplacement of ejecta, the innermost ring faults attain their maximum offset before the outermost faults, and the last ring structure to form is the inner basin ring, which is not a ring fault and instead forms by dynamic collapse of the central uplift similar to peak rings of smaller basins (Kring et al., 2016; Morgan et al., 2016).

3.2. Impactor Size

Here we explore the role of impactor size on the formation of basins and their rings by comparing simulations with impactor diameters of 40, 50, 60, and 70 km and keeping all target parameters the same as our fiducial model. We first discuss the role of impactor size on the location of outer ring faults then the location of the inner basin ring (peak ring). Finally, we consider how impactor size affects the final crustal structure of the basin.

The 40-km-diameter impactor produces a basin with only one ring fault with kilometer-scale offset (Figure 5a). This basin is ~550 km in diameter, and the ring fault comes to the surface very near the crater rim. This basin therefore seems to be more consistent with a peak-ring basin than a multiring basin. The 50-km-diameter impactor produces an ~700-km diameter basin with two ring faults that have a spacing of ~50 km, a structure more similar to multiring basins (Figure 5b). Thus, our simulations suggest that there is a transition from peak-ring to multiring basins for basin diameters between 500 and 700 km. This is consistent with the observed transition to multiring structures at ~600 km in diameter. According to Neumann et al. (2015), the smallest lunar multiring basin is the 571-km-diamter Hertzsprung basin and above ~650-km-diameter most basins are multiring basins. Ring tectonic theory predicts that if the lithosphere is too strong or too thick, with respect to the scale of the collapsing crater, ring faults cutting through the lithosphere will not form (McKinnon & Melosh, 1980; Melosh, 1982). For small craters this may be true, but even our simulated peak-ring basin (Figure 5a) has a fault that cuts to ~80-km deep, similar to the depth of the weakest material in our model (Figure 1). Simulations of the ~320-km Schrödinger basin also exhibit

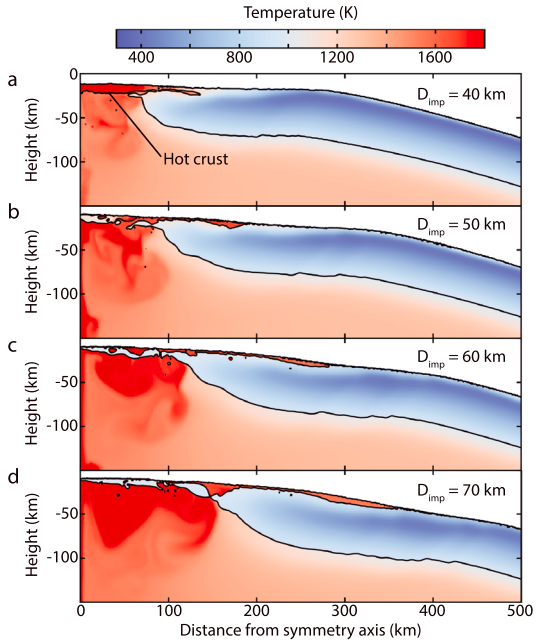

Figure 7. Effect of impactor size on final basin temperature structure. Material is colored according to temperature as indicated by the scale bar. Initial impact occurs at the origin. The thin black curves are the boundary or interface between two materials including, crust, mantle, and void. In general, crust and mantle can be identified as cooler and hotter materials, respectively. Other than impactor size, as indicated, all other parameters are the same as in the fiducial model.

a fault that cuts to depth of ~80 km (Kring et al., 2016). Thus, contrary to arguments of McKinnon and Melosh (1980), ring tectonic theory likely also applies to the single ring fault that defines the rim of peak-ring basins, as well as to multiring basins.

Figure 5 shows the resultant ring structures made by each impact, Table 3 summarizes the results of ring locations at the surface, and Figure 6 shows a comparison to the ring location of observed basins. We note that although the locations of ring faults in our models are well defined, there is about 10–20-km uncertainty in the location of the peak-ring, which can be quite broad. This uncertainty corresponds to ±0.2 in the ring ratios for the 50-km-diameter impactor simulation. Figure 6a shows that our models reproduce the ratio of the diameter of the outer ring to the peak ring reasonably well. Observed basins exhibit a ratio of peak ring to crater rim diameter of about 3 for the smallest basins and decreases to less than 2 for the largest basins (Figure 6a). Our simulations show a similar trend. We also note that the ratio between the first outer ring (the middle ring of multiring basins or the rim of peak-ring basins) and the peak ring increases dramatically with decreasing basin diameter, from the oft-cited $\sqrt{2}$ ratio for large multiring basins (Figure 6b) to a ratio of 2–3 for peak-ring basins (Figure 6a, blue triangles). Our model results predict a very similar trend, though they exhibit a larger ratio across all diameters. The largest outlier in all frames is the basin produced by the 50-km-diameter impactor, which is near the transition from peak-ring to multiring structures. In our simulations, the middle ring (first ring fault) tends to be too far from the peak ring (Figure 6b) and too close to the outer ring fault (basin rim) (Figure 6c). Although this spacing does not agree with observations, we note that the spacing and location of rings are very sensitive to target thermal structure as we demonstrate in the following section. In the case of the 60- and 70-km-diameter impactors there are three faults with kilometer-scale offsets (Figures 5c and 5d) where only two dominant ring faults are expected. The appearance of more large-scale faults than expected and the disagreement with the location of the inner ring fault (Figures 6b and 6c) indicates that our simulations may not reproduce fault spacing accurately, and model developments that may improve accuracy are discussed in section 4.

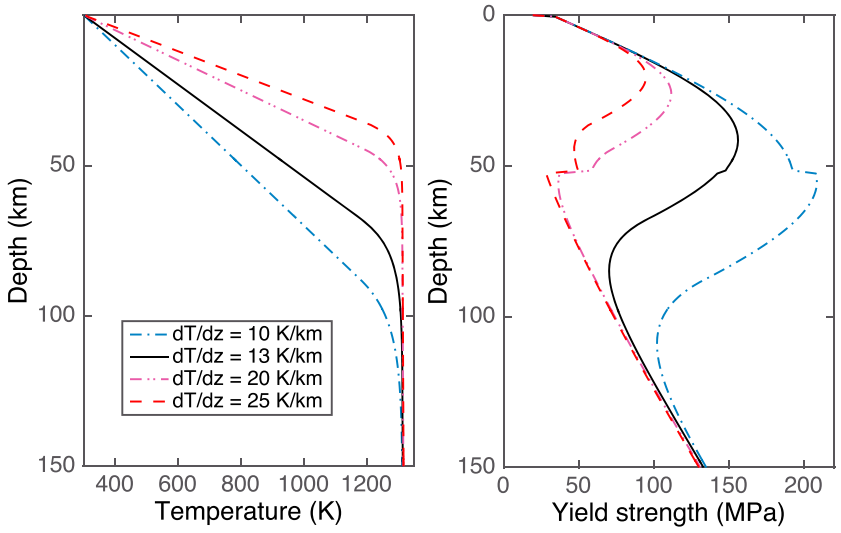

Figure 8. (left) Preimpact temperature and (right) material strength as a function of depth in the target for different preimpact thermal gradients as indicated in the legend. All other parameters are the same as in the fiducial model.

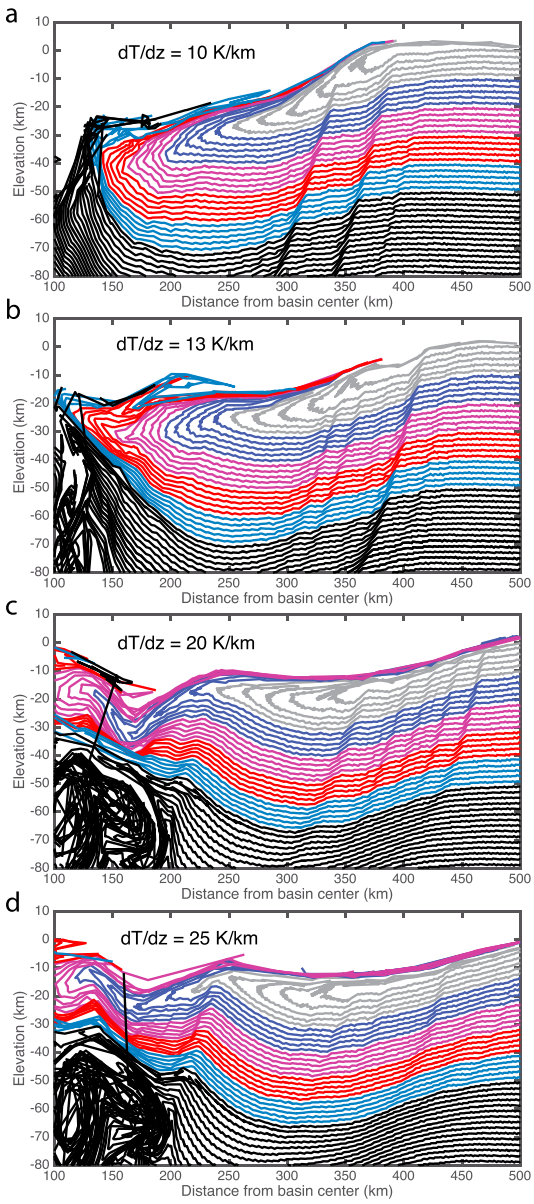

Figure 9. Vertically exaggerated plot demonstrating how target thermal gradient affects ring spacing and location. For more information about these plots see Figure 3. All frames are plotted 50 min after impact. Note that the horizontal axis starts at 100 km for all frames. Other than preimpact thermal gradient, as indicated, all other parameters are the same as in the fiducial model.

Figure 7 shows the final basin temperature structure. As the impactor size increases, the mantle plug or inner region of thinned crust increases in scale and the location of the thickened annulus of crust shifts outward consistent with the work of Potter et al. (2012) and Miljkovic et al. (2016). In all cases, crustal material migrates inward and covers the basin center. The crustal cap is hotter for smaller impactors, but the thickness of this crustal cap is insensitive to impactor size, consistent with the findings of Freed et al. (2014). Smaller impacts do not excavate material from as great a depth as the larger impactors do. Thus, much of the hotter, potentially molten, shock-heated crustal material produced during the D_{imp} = 40-km simulation remains within or near the transient crater and readily migrates to the basin center. During the D_{imp} = 70-km simulation hot shock-heated crustal material is ejected to great distances and is unable to migrate to the basin center. The greater excavation depth of larger impacts also results in more mantle material being splashed out from the crater during collapse of the central uplift. The scale of the melt pool increases with impactor size as expected (Pierazzo et al., 1997).

3.3. Thermal Gradient

Here we explore the role of thermal gradient on the formation of basins and their rings by comparing simulations with thermal gradients of 10, 13, 20, and 25 K/km and keeping all other target parameters and the impactor parameters the same as our fiducial model. We first discuss how thermal gradient (*dT*/*dz*) affects preimpact target strength. Then we discuss how *dT*/*dz* affects the location and formation of outer ring faults. Finally, we consider how *dT*/*dz* affects the location of the inner basin ring (peak ring) and the final crustal structure of the basin.

Figure 8 shows the four thermal gradients we consider and how they affect material strength. Discontinuities in the slope of the material strength profile (Figure 8b) mark the transition from crust to mantle material at a depth of 52 km. Because the temperature of these simulations all follow nearly the same adiabat at ~1,300 K at a depth of ~140 km (Figure 8a), the preimpact strength at depths exceeding 140 km is nearly the same for all the models (Figure 8b). Although we nominally set all models to follow an adiabat at ~1,300 K, the *dT*/*dz* = 25-K/km model begins following the ~0.045-K/km adiabatic gradient ~100 km shallower than the *dT*/*dz* = 10-K/km model. Thus, at 150-km depth, the model with *dT*/*dz* = 25-K/km model is 4.36 K hotter than the model with *dT*/*dz* = 10 K/km. Smaller differences occur for the other thermal gradients considered. At all depths, the overburden pressure is slightly lower for models with higher thermal gradients because our equation of state requires that the hotter material is slightly less dense. At 150-km depth, the pressure in the *dT*/*dz* = 25-K/km

Table 4
Location of Ring Structures on Simulated Basin Showing Effect of Thermal Gradient

Thermal gradient (K/km)	Peak ring diameter (km)	Inner ring fault diameter (km)	Outer ring fault diameter (km)
10	280 (?)	700	790
13	410	700	845
20	495	750	950
25	500	665?	885?

Note. Question marks indicate ring locations that are uncertain as indicated in the text.

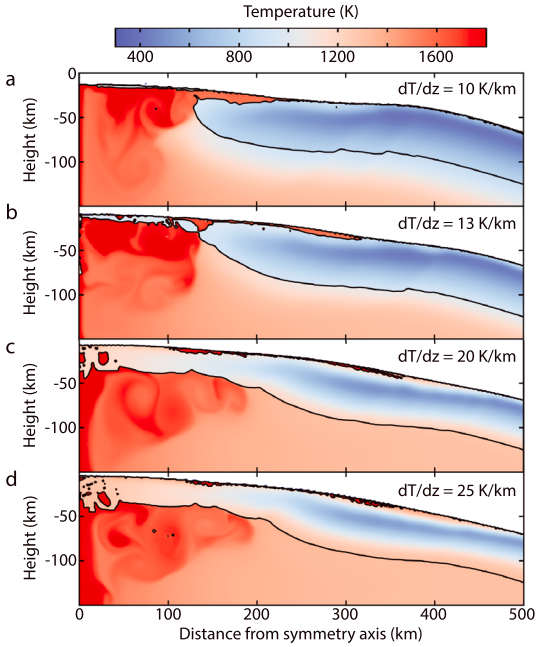

Figure 10. Effect of preimpact target thermal gradient on final basin structure. Material is colored according to temperature as indicated by the scale bar. Initial impact occurs at the origin. The thin black curves are the boundary or interface between two materials including crust, mantle, and void. In general, crust and mantle can be identified as cooler and hotter materials, respectively. Other than target thermal gradient, as indicated, all other parameters are the same as in the fiducial model.

model is 5.8 MPa lower than the model with dT/dz = 10 K/km. Material strength depends on both pressure and temperature. Thus, our models with a higher thermal gradient are slightly weaker at depths exceeding ~140 km (Figure 8). These realistic effects are minor, resulting in a strength difference of 4.8 MPa (~4%) between the 10- and 25-K/km models at 150-km depth.

Figure 9 shows the resultant ring structures made by each impact, and Table 4 summarizes the results of ring location at the surface. The location of the innermost ring fault does not have a strong dependence on dT/dz, while the outermost ring fault tends to move outward as dT/dz increases (for dT/dz = 25 K/km the outermost ring fault is difficult to define). The 10-K/km thermal gradient has the thickest and strongest lithosphere (Figure 8). This results in collapse of the transient crater being accommodated by inward flow and upward flow of material relatively close to the basin center and from relatively large depth. As the thermal gradient increases, more collapse of the crater is accommodated by inward flow of material that is shallower and farther from the basin center. This in turn produces a larger region of crustal material being pulled down and in toward the basin center. This explains the increasing distance of the outermost ring fault as thermal gradient increases.

In addition to an outward shift of the outermost fault, we also find that as the thermal gradient increases, the number of faults increases and fault offsets decrease. There are two, three, and four to five faults in the 10-, 13-, and 20-K/km simulations, respectively. In the 25-K/km model faults are difficult to discern from more widely distributed plastic strain. The appearance of more faults is the result of the lithosphere becoming thinner as dT/dz increases. This aspect of our simulation is consistent with ring tectonic theory, which predicts that a thicker lithosphere will result in larger ring spacing and a thinner lithosphere will result in more numerous closely spaced faults as observed on Callisto and Ganymede (McKinnon & Melosh, 1980). In addition to thinning, the lithosphere also becomes weaker as dT/dz increases. This likely explains why there is more distributed plastic strain between faults for higher thermal gradients.

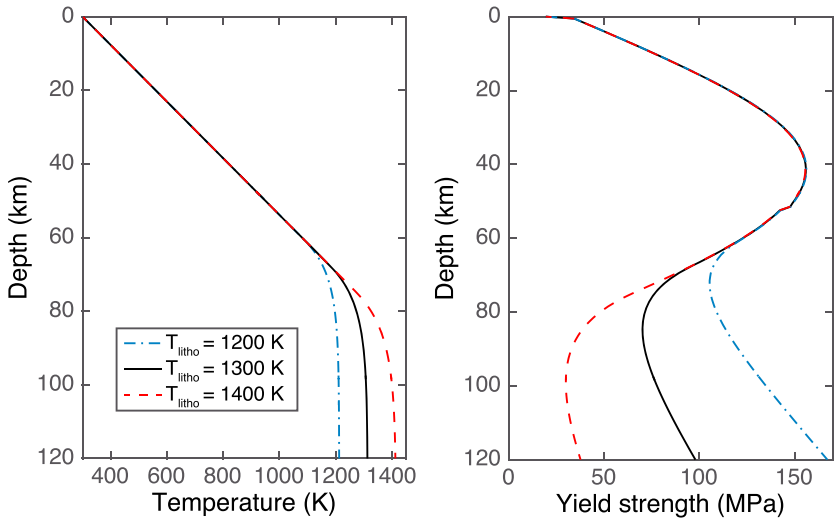

Figure 11. (left) Preimpact temperature and (right) material strength as a function of depth in the target for different temperatures at the base of the lithosphere as indicated in the legend. All other parameters are the same as in the fiducial model.

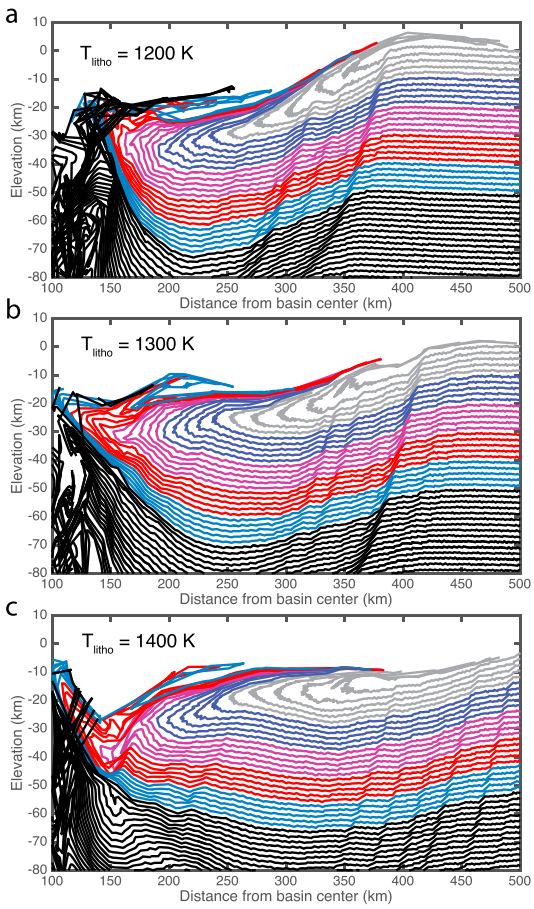

Figure 12. Vertically exaggerated plot demonstrating how temperature at the base of the lithosphere affects ring spacing and location. For more information about these plots see Figure 3. All frames are plotted 50 min after impact. Note that the horizontal axis starts at 100 km for all frames. Other than temperature at the base of the target's lithosphere, as indicated, all other parameters are the same as in the fiducial model.

We find that the position of the innermost basin ring (peak ring) moves outward as *dT/dz* increases (Table 4 and Figure 9). For higher thermal gradients, crustal material is weaker and is more easily pushed up and outward as the central uplift collapses (Figures 2c and 2d) allowing the peak ring to form farther from the basin center. For *dT/dz* = 25 K/km the subsequent inward collapse of the bulge, produced by collapse of central uplift, actually produces a ring fault that defines the location of the peak ring (Figure 9d). Similar yet weaker localization can be seen in the 13- and 20-K/km models (Figures 9b and 9c). The topographic expression of the Inner Rook seems inconsistent with such a ring fault (e.g., Nahm et al., 2013). However, a kink or discontinuity in the curvature of the crust-mantle interface like that seen in the 13-, 20-, and 25-K/km models (Figures 9b–9d and 10b–10d) is consistent with gravity signature of Orientale's Inner Rook Ring (Zuber et al., 2016). Gravity gradient maps and profiles of Orientale show a pair of strong positive and negative gravity gradients interior to the Inner Rook (Andrews-Hanna et al., 2018). The positive anomaly indicates a downward concavity at the crust-mantle interface, consistent with the kink in the simulated crust-mantle interface, while the negative anomaly does not have an obvious parallel in the models.

Figure 10 shows the postimpact thermal structure of basins produced with different thermal gradients. We find that as *dT/dz* is increased, the zone of crustal thinning becomes larger and the location of the thickened crustal annulus moves outward consistent with previous work (Miljkovic et al., 2016; Potter et al., 2012). As thermal gradient is increased, the cap of crustal material covering the basin center becomes thicker. An incomplete, thin crustal cap is produced if *dT/dz* = 10 K/km (Figure 10a), whereas an ~30-km-thick crustal cap is produced when *dT/dz* = 25 K/km. For high thermal gradients, crustal material is warmer and weaker (Figure 8) and more readily flows inward to cover the basin center. This is consistent with previous simulations of smaller basins (Freed et al., 2014).

3.4. Temperature at Depth

Here we explore the role of the temperature of warm mantle material beneath the lithosphere on the formation of basins and their rings by comparing simulations with this temperature set to 1,200, 1,300, and 1,400 K and keeping all other target parameters and impactor parameters the same as our fiducial model. We first discuss how the temperature of warm mantle material (T_{litho}) affects preimpact target strength. Then we discuss how T_{litho} affects the location and formation of outer ring faults. Finally, we consider how T_{litho} affects the location of the inner basin ring (peak ring) and the final crustal structure of the basin.

Figure 11 shows the three temperature-depth profiles we consider and how they affect material strength. Because the temperature-depth profiles of our simulations all follow a thermal gradient of 13 K/km from the surface, all three models have identical temperatures and nearly identical material strengths to a depth of ~60 km. Below this depth the three models diverge; at a depth of 120 km the T_{litho} = 1,200-, 1,300-, and 1,400-K models have preimpact strengths of 167, 98, and 38 MPa, respectively. The slight differences in strength at depths less than 60 km are caused by small differences in surface gravity and therefore overburden pressures between these models. Surface gravity is calculated in a self-consistent way from the distribution of mass in our target body. Material densities depend on pressure and temperature, so a Moon-like target with a colder mantle is slightly denser and has a higher surface gravity than a target with a warmer mantle.

Figure 12 shows the resultant ring structures made by each impact, and Table 5 summarizes the results of ring locations at the surface. Although

Table 5
Location of Ring Structures on Simulated Basin Showing Effect of Temperature of Warm Mantle Material

T_{litho} (K/km)	Peak ring diameter (km)	Inner ring fault diameter (km)	Outer ring fault diameter (km)
1,200	390	660	790
1,300	410	700	845
1,400	420	800	1,000

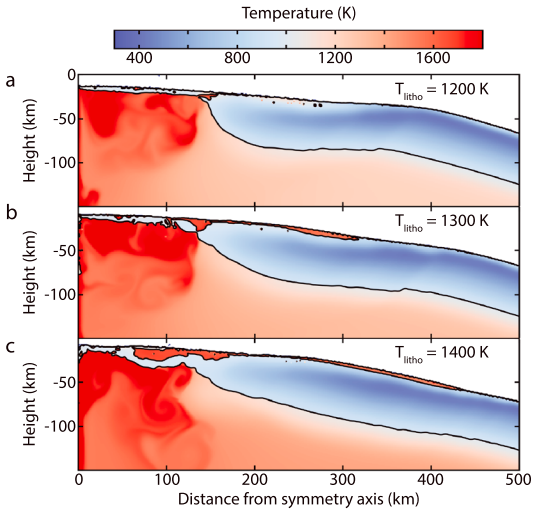

Figure 13. Effect of temperature at the base of the lithosphere on final basin structure. Material is colored according to temperature as indicated by the scale bar. Initial impact occurs at the origin. The thin black curves are the boundary or interface between two materials including crust, mantle, and void. In general, crust and mantle can be identified as cooler and hotter materials, respectively. Other than temperature at the base of the target's lithosphere, as indicated, all other parameters are the same as in the fiducial model.

the strength profiles produced by varying T_{litho} differ substantially from those produced by varying dT/dz (Figures 8 and 11), the resultant ring and basin structures display some striking similarities (Figures 9 and 12). As T_{litho} is increased, both the innermost and outermost ring faults move outward (for dT/dz the location of the innermost fault remained relatively constant). The T_{litho} = 1,200-K simulation has the strongest asthenosphere (Figure 11). This results in collapse of the transient crater being accommodated by inward and upward flows of material relatively close to the basin center and originating from a relatively large depth. As T_{litho} is increased, more collapse of the crater is accommodated by inward flow of material farther from the basin center. This in turn produces a larger region of crustal material being pulled down and in toward the basin center. This explains the increasing distance of the outermost ring fault as T_{litho} is increased.

There are three large-scale faults cutting through the crust for all values of T_{litho}. For T_{litho} = 1,400 K there are five large-scale faults apparent, but two of these faults begin at depths of ~20 km and would not correspond to topographic basin rings (Figure 12c). The offset along faults is reduced as the temperature of the mantle is increased (Figure 12). As T_{litho} is increased, the asthenosphere becomes weaker and flows more readily (Figure 11). For T_{litho} = 1,200 K the collapse of the transient crater is accommodated by large strains relatively close to the transient crater rim, whereas for T_{litho} = 1,400 K crater collapse is accommodated by lower overall strain from a greater distance. As T_{litho} is increased, there is also likely less basal traction on the lithosphere. Thus, the total fault offsets and inward collapse of lithospheric material is reduced as the asthenosphere becomes weaker and flows more readily.

We find that the position of the innermost basin ring (peak ring) moves outward as mantle temperature is increased (Table 5). For higher T_{litho} material more readily collapses inward and produces a larger central uplift (e.g., Figure 2b). The peak ring forms as the result of collapse of the central uplift, and the larger central uplift leads to a larger peak ring diameter. There is also significantly more mantle splash at higher T_{litho} (Figure 13). In the final basin structure, the transition from thin crust near the basin center to the thickened annulus is more abrupt for lower mantle temperatures (Figure 13). The thickening of crust in the annulus is also more distributed for higher T_{litho}. These effects together result in an outward shift in the location of the thickened annulus for higher T_{litho}. The thickness of the crustal cap is somewhat higher for higher $T_{litho,}$ but the effect is quite limited compared to the effect of changes in dT/dz (Figures 10 and 13).

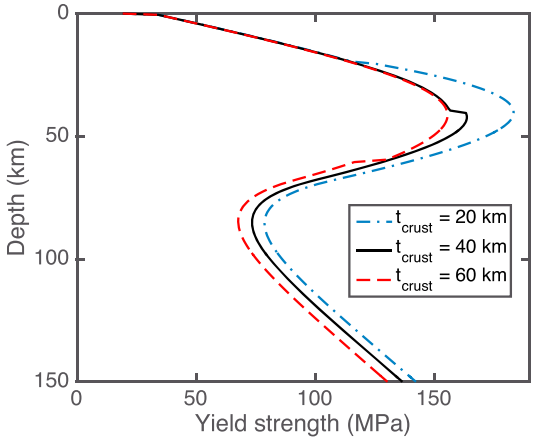

Figure 14. Material strength as a function of depth in the target for different crustal thicknesses as indicated in the legend. All other parameters are the same as in the fiducial model.

3.5. Crustal Thickness

Here we explore the role of crustal thickness on the formation of basins and their rings by comparing simulations with crusts that are 20-, 40-, and 60-km thick while keeping all other target parameters and impactor parameters the same as our fiducial model. We first discuss how crustal thickness (t_{crust}) affects preimpact target strength. Then we discuss how t_{crust} affects the location and formation of outer ring faults. Finally, we consider how t_{crust} affects the location of the inner basin ring (peak ring) and the final crustal structure of the basin.

Figure 14 shows the effect of crustal thickness on target strength. We do not include the target thermal profiles as they are identical to the fiducial model (Figure 1). Although these models have the same temperature profile, at 85-km depth the models with 20-, 40-, and 60-km-thick crusts have strengths of 79, 73, and 68 MPa, respectively. Our crustal material has a density of ~2,600 kg/m^3, while the mantle has a density of ~3,300 kg/m^3,

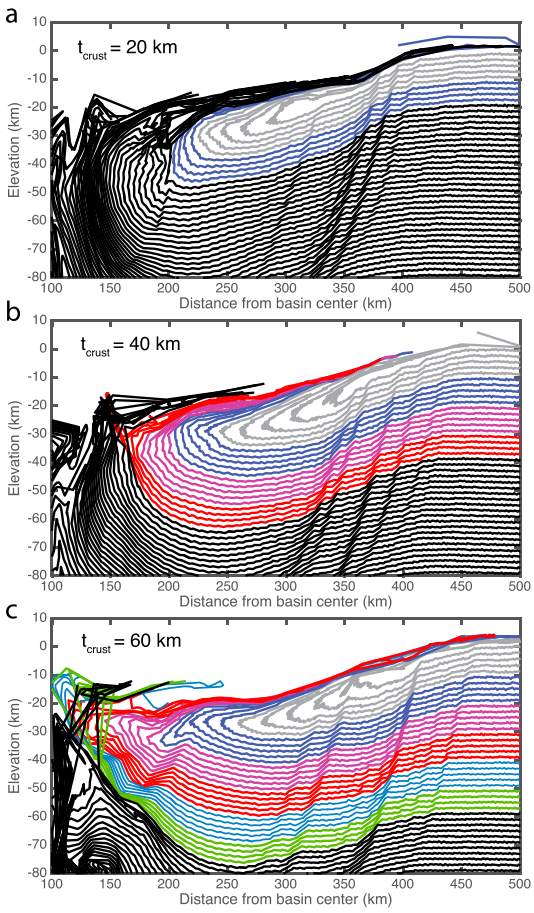

Figure 15. Vertically exaggerated plot demonstrating how crustal thickness affects ring spacing and location. For more information about these plots see Figure 3. Note that the horizontal axis starts at 100 km for all frames. Other than target crustal thickness, as indicated, all other parameters are the same as in the fiducial model.

and these densities depend on temperature and pressure. Thus, the thin crust model has a higher overburden pressure than the other models at depths exceeding 20 km. This difference in overburden pressure explains the difference in strength of mantle material in the models. Slight differences in strength at depths less than 20 km are caused by small differences in surface gravity (a Moon-like target with a thicker crust is slightly less dense and has a lower surface gravity than a Moon-like target with a thinner crust). Note that the comparison in Figure 14 does not illustrate the fact that the mantle includes a viscoelastic-plastic rheology, whereas the crust is described by a simpler elastic-plastic rheology.

Figure 15 shows the resulting ring structures made by each impact. For the 20-km-thick crust, the vast majority of the fault offset occurs on closely spaced ring faults at 380 and 400 km (Figure 15a). There is an inner fault located at ~335 km, but this fault has a smaller offset and only extends to depth of ~60 km (Figure 15a). As the crustal thickness is increased, the spacing between faults with the largest offsets increases (Figure 15). The strength differences between the models with t_{crust} = 40 and 60 km are minor, and the observed trend does not agree with the general intuition gained from exploring the effect of differences in dT/dz on ring fault spacing. We expect increasing strength of the lithosphere to lead to larger offsets and larger spacing between individual faults. Differences in the effects of dilatancy between the crustal and mantle material may explain the differences seen in Figure 15. Although we use the same dilatancy parameters for the crust and mantle, our mantle strength profiles use a melt temperature or 1,373 K consistent with the mantle solidus, while the crust uses a melt temperature of 1,513 K, which is more consistent with the liquidus of crustal material. The dilatancy model we employ assumes that materials are less dilatant as their melt temperature is approached (Collins, 2014). Thus, at the same material temperature mantle material is less dilatant than crustal material. Because dilatancy has a localizing effect (Montési, 2002), localization occurs more readily in the crust and a thicker crust results in more localization. This is consistent with the greater spacing of large offset faults found for the thickest crust and the truncation of the innermost fault in the case of the 20-km-thick crust. It is also possible that the use of a viscoelastic-plastic rheology in the mantle and an elastic-plastic-rheology in the crust contributes to the differences shown in Figure 15. Because the strength of the lower crust and upper mantle is very similar in our numerical simulations (Figure 14), we did not expect that the formation of basin rings would be sensitive to crustal thickness. Basin ring formation in our simulations, however, is sensitive to crustal thickness and the rheological differences between crust and mantle outlined above. It is not clear whether this aspect of our simulations is supported by observations.

The innermost basin ring or peak ring has a diameter of 410 km for the model with a 60-km-thick crust. For the t_{crust} = 20- and 40-km simulations, the bulge of material produced by collapse of the central uplift occurs purely in mantle material and no lasting peak ring is produced. Mantle material is exposed over much of the basin for the simulations with 20- and 40-km-thick crusts (Figures 16a and 16b). For the simulation with a 60-km-thick crust, a crustal cap covers the basin center (Figure 16c) and is thicker than the crustal cap produced in the fiducial model (Figure 10b). Material with temperature less than ~1,000 K has roughly the same final location in all simulations (Figure 16). The basins in Figures 16a and 16b show a similar structure of exposed mantle material overlying downward displaced crust outside of the excavation cavity and an absence of a peak ring as seen in our simulation with the lowest thermal gradient (dT/dz = 10 K/km, Figures 9a and 10a). Our simulation with the lowest mantle temperature also has a similar structure, lacking a peak ring (T_{litho} = 1,200 K, Figures 12a). Thus, we expect that if we used a higher thermal gradient and higher mantle temperature more appropriate for basins in or near the PKT, a crustal cap and lasting peak ring could be produced even for t_{crust} = 20 and 40 km.

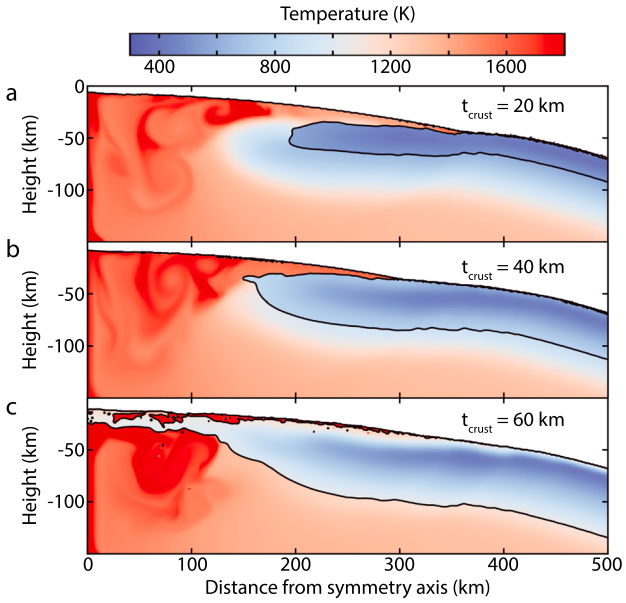

Figure 16. Effect of crustal thickness on final basin structure. Material is colored according to temperature as indicated by the scale bar. Initial impact occurs at the origin. The thin black curves are the boundary or interface between two materials including crust, mantle, and void. In general, crust and mantle can be identified as cooler and hotter materials, respectively. Other than temperature at the base of the target's lithosphere, as indicated, all other parameters are the same as in the fiducial model.

4. Discussion

Although our simulations provide insight into the formation of multiring basins, a few features of our simulations are not consistent with observed basins. Our simulations tend to have a ratio between the outermost ring fault and innermost ring fault that is smaller than expected and between the innermost ring fault and the peak ring that is larger than expected (Neumann et al., 2015; Wilhelms, 1987). Our simulations with higher T_{litho} or higher dT/dZ have larger spacing between the innermost and outermost ring faults but tend to have smaller fault offsets and potentially too many faults in the case of dT/dz. It is possible that setting T_{litho} between 1,300 and 1,400 K combined with dT/dz between 13 and 20 K/km could produce a larger fault spacing while keeping fault offsets high and the number of faults to two or three. It is interesting to note that a larger crustal thickness seems to produce larger fault spacing, and this is attributed to the crustal rheology being more localizing. It is possible that a more localizing rheology throughout the target could produce ring structures that better match observations.

One way to increase the amount of localization would be to include a fault-weakening model, which might include rate-weakening (Senft & Stewart, 2009), localized shear heating (Crawford & Schultz, 2013), or acoustic fluidization (Hay et al., 2014). Nevertheless, even without these more exotic rheologies, we are able to resolve the formation of basin rings. We may also see improvement in our simulations if resolution is increased. We note, however, that the 1-km-resolution simulations shown here each took ~1 month to complete on a high-specification workstation.

Our smallest simulated crater is an ~500-km-diamter peak-ring basin. The rim of this basin is associated with a ring fault that cuts through the lithosphere (to a depth of ~80 km). Simulations of the smaller ~320-km-diameter Schrödinger basin, which is also a peak-ring basin, also have a rim associated with a single ring fault cutting to a depth of ~80 km (Kring et al., 2016). This structure suggests that ring tectonic theory (McKinnon & Melosh, 1980) may also apply to the ring faults that define the rims of peak-ring basins. We note that neither our simulations nor those of Kring et al. (2016) resolve the terrace zones of these peak-ring basin. Additionally, there is no morphologic distinction between the terrace zones of small complex craters, where such lithospheric-scale faults are unlikely and do not occur in simulations (Yue et al., 2013), and the observed terrace zones of peak-ring basins. Thus, it is difficult to say whether the lithosphere-scale faults seen in Kring et al. (2016) and our simulations of peak-ring basins would remain if terracing was resolved. Further analysis of GRAIL gravity data could reveal whether such deep faults predicted by modeling are present in large peak ring basins.

Best fitting forward models of gravity gradients and crustal thickness models indicate that the Orientale's Outer Rook Ring is nearly vertical at some azimuths (Andrews-Hanna et al., 2018). None of our simulations produce ring faults that are significantly steeper than ~60°, a finding consistent with Anderson's theory of faulting (Anderson, 1905). It is possible that the inclusion of a crustal fault-weakening rheology would produce steeper faults. It is well known that most impacts are oblique, with the most likely impact angle being 45°. We expect that the slightly asymmetric collapse of the transient crater made by an oblique impact (Elbeshausen et al., 2009) would likely produce some uprange-downrange ring asymmetries. It is conceivable that oblique impacts could produce more vertical ring faults for some azimuths, but it is not clear how this would occur. Direct exploration of the effect of impact obliquity would require full three-dimensional simulations at the same 1-km spatial resolution, which are computationally prohibitive at the moment.

Our simulations show that the process of basin ring formation is sensitive to target thermal structure and possibly crustal thickness. In actuality, basin ring formation is sensitive to material rheology, which is related to material temperature and pressure through a strength model. Thus, a best fitting target thermal structure is only as realistic as our material strength and rheological models. Although our simulations are far from a complete description of the formation of multiring basins, using the intuition gained about the controls on

multiring basin formation, it should be possible to produce simulations that simultaneously match the crustal thickness of observed basins and their approximate ring locations. Coupled with detailed gravity analyses (Andrews-Hanna et al., 2018), these simulations would provide valuable insight into the process of basin ring formation. Additionally, if basins of various location and ages are compared, we could estimate how the thermal structure of the Moon varied with time and location on the Moon during the basin forming epoch.

5. Conclusions

We have simulated the formation of lunar multiring basins under a wide range of conditions. We have explored the effects of impactor size, crustal thickness, near-surface thermal gradient, and temperature of deeper material. Generally, we find that outer basin rings are large normal faults that form during crater collapse and that the location and spacing of basin rings is sensitive to target rheology. We find that the inward flow of warm weak material at depth is paramount to the formation of these rings, a conclusion that agrees with ring tectonic theory (Melosh & McKinnon, 1978). Our simulations also indicate that the rims of peak-ring basins may form in a similar way to the outer rings of multiring basins.

Our simulations successfully produce peak-ring and multiring basins, similar to those observed on the Moon. In addition to reproducing the approximate spacing and offsets of the rings in Orientale, as noted previously (Johnson et al., 2016), the model results reproduce a number of other important observations. The predicted transition diameter from peak-ring to multiring basins between diameters of 500 and 700 km agrees well with the observed transition between 570 and 650 km. The models also predict the observed difference in the ratio between the diameters of the first outer ring and the peak ring for peak-ring and multiring basins (~2 and ~1.4, respectively).

Acknowledgments
We thank W. B. McKinnon and an anonymous referee for their helpful comments. We thank the developers of iSALE, including Kai Wünnemann, Dirk Elbeshausen, Tom Davison, and Boris Ivanov. Some plots in this work were created with the pySALEPlot tool written by Tom Davison. B. C. J. was supported by grant 80NSSC17K0341 from the NASA Lunar Data Analysis Program. G. S. C. was supported by UK Science and Technology Facilities Council grant ST/N000803/1. The iSALE code is not open access; it is distributed on a case-by-case basis to academic users in the impact community, strictly for noncommercial use. Scientists interested in using or developing iSALE should see www.isale-code.de for details of how to request access. Model input and output from this work are available at the Harvard Dataverse, https://doi.org/10.7910/DVN/JUCVXW.

References

Amsden, A. A., Ruppel, H. M., & Hirt, C. W. (1980). SALE: A simplified ALE computer program for fluid flow at speeds. Los Alamos National Laboratories Report LA-8095.

Anderson, E. M. (1905). The dynamics of faulting. *Transactions. Edinburgh Geological Society*, *8*(3), 387–402. https://doi.org/10.1144/transed.8.3.387

Andrews-Hanna, J. C., Head, J. W., Johnson, B. C., Keane, J. T., Kiefer, W. S., McGovern, P. J., et al. (2018). Ring faults and ring dikes around the Orientale basin on the Moon. *Icarus*, *310*, 1–20. https://doi.org/10.1016/j.icarus.2017.12.012

Baker, D. M. H., Head, J. W., Fassett, C. I., Kadish, S. J., Smith, D. E., Zuber, M. T., & Neumann, G. A. (2011). The transition from complex crater to peak-ring basin on the Moon: New observations from the Lunar Orbiter Laser Altimeter (LOLA) instrument. *Icarus*, *214*(2), 377–393. https://doi.org/10.1016/j.icarus.2011.05.030

Collins, G. S. (2014). Numerical simulations of impact crater formation with dilatancy. *Journal of Geophysical Research: Planets*, *119*, 2600–2619. https://doi.org/10.1002/2014JE004708

Collins, G. S., Melosh, H. J., & Ivanov, B. A. (2004). Modeling damage and deformation in impact simulations. *Meteoritics & Planetary Science*, *39*(2), 217–231. https://doi.org/10.1111/j.1945-5100.2004.tb00337.x

Crawford, D. A., & Schultz, P. H. (2013). A model of localized shear heating with implications for the morphology and paleomagnetism of complex craters. Large Meteorite Impacts and Planetary Evolution V, #3047.

Dence, M. R. (1965). The extraterrestrial origin of Canadian craters. *Annals of the New York Academy of Sciences*, *123*(2), 941–969. https://doi.org/10.1111/j.1749-6632.1965.tb20411

Elbeshausen, D., & Melosh, J. (2018). A nonlinear and time-dependent visco-elasto-plastic rheology model for studying shock-physics phenomena. Arxiv.org.

Elbeshausen, D., Wünnemann, K., & Collins, G. S. (2009). Scaling of oblique impacts in frictional targets: Implications for crater size and formation mechanisms. *Icarus*, *204*(2), 716–731. https://doi.org/10.1016/j.icarus.2009.07.018

Freed, A. M., Johnson, B. C., Blair, D. M., Melosh, H. J., Neumann, G. A., Phillips, R. J., Solomon, S. C., et al. (2014). The formation of lunar mascon basins from impact to contemporary form. *Journal of Geophysical Research: Planets*, *119*, 2378–2397. https://doi.org/10.1002/2014JE004657

Garrick-Bethell, I., & Zuber, M. T. (2009). Elliptical structure of the lunar South Pole-Aitken basin. *Icarus*, *204*(2), 399–408. https://doi.org/10.1016/j.icarus.2009.05.032

Hay, H. C. F. C., Collins, G. S., & Davison, T. M. (2014). Complex crater collapse: A comparison of the block and Melosh models of acoustic fluidization. 45th Lunar and Planetary Science Conference, 45, 1938.

Hiesinger, H., & Head, J. W. (2004). Lunar South Pole-Aitken impact basin: Topography and mineralogy. Th Lunar and Planetarry Science Conference, #1164.

Ivanov, B. A., Melosh, H. J., & Pierazzo, E. (2010). Basin-forming impacts: Reconnaissance modeling. *Geological*, 29–49. https://doi.org/10.1130/2010.2465(03)

Johnson, B. C., Blair, D. M., Collins, G. S., Melosh, H. J., Freed, A. M., Taylor, G. J., et al. (2016). Formation of the Orientale lunar multiring basin. *Science*, *354*(6311), 441–444. https://doi.org/10.1126/science.aag0518

Kring, D. A., Kramer, G. Y., Collins, G. S., Potter, R. W. K., & Chandnani, M. (2016). Peak-ring structure and kinematics from a multi-disciplinary study of the Schrödinger impact basin. *Nature Communications*, *7*, 13161. https://doi.org/10.1038/ncomms13161

Laneuville, M., Wieczorek, M. A., Breuer, D., & Tosi, N. (2013). Asymmetric thermal evolution of the Moon. *Journal of Geophysical Research: Planets*, *118*, 1435–1452. https://doi.org/10.1002/jgre.20103

Le Feuvre, M., & Wieczorek, M. A. (2011). Nonuniform cratering of the Moon and a revised crater chronology of the inner solar system. *Icarus*, *214*(1), 1–20. https://doi.org/10.1016/j.icarus.2011.03.010

McKinnon, W. B., & Melosh, H. J. (1980). Evolution of planetary lithospheres: Evidence from multiringed structures on Ganymede and Callisto. *Icarus*, *44*(2), 454–471. https://doi.org/10.1016/0019-1035(80)90037-8

Melosh, H. J. (1982). A simple mechanical model of Valhalla basin, Callisto. *Journal of Geophysical Research*, *87*(B3), 1880–1890. https://doi.org/10.1029/JB087iB03p01880

Melosh, H. J. (1985). Ejection of rock fragments from planetary bodies. *Geology*, *13*(2), 144–148. https://doi.org/10.1130/0091-7613(1985)13<144:EORFFP>2.0.CO;2

Melosh, H. J. (1989). *Impact cratering: A geologic process*. New York: Oxford University Press.

Melosh, H. J., & Ivanov, B. A. (1999). Impact crater collapse. *Annual Review of Earth and Planetary Sciences*, *27*(1), 385–415. https://doi.org/10.1146/annurev.earth.27.1.385

Melosh, H. J., & McKinnon, W. B. (1978). The mechanics of ringed basin formation. *Geophysical Research Letters*, *5*(11), 985–988. https://doi.org/10.1029/GL005i011p00985

Miljkovic, K., Collins, G. S., Wieczorek, M. A., Johnson, B. C., Soderblom, J. M., Neumann, G. A., & Zuber, M. T. (2016). Subsurface morphology and scaling of lunar impact basins. *Journal of Geophysical Research: Planets*, *121*, 1695–1712. https://doi.org/10.1002/2016JE005038

Miljkovic, K., Wieczorek, M. A., Collins, G. S., Laneuville, M., Neumann, G. A., Melosh, H. J., et al. (2013). Asymmetric distribution of lunar impact basins caused by variations in target properties. *Science*, *342*(6159), 724–726. https://doi.org/10.1126/science.1243224

Montési, L. G. J. (2002). A unified description of localization for application to large-scale tectonics. *Journal of Geophysical Research*, *107*(B3), 2045. https://doi.org/10.1029/2001JB000465

Morgan, J. V., Gulick, S. P. S., Bralower, T., Chenot, E., Christeson, G., Claeys, P., et al. (2016). The formation of peak rings in large impact craters. *Science*, *354*(6314), 878–882. https://doi.org/10.1126/science.aah6561

Nahm, A. L., Öhman, T., & Kring, D. A. (2013). Normal faulting origin for the Cordillera and Outer Rook Rings of Orientale Basin, the Moon. *Journal of Geophysical Research: Planets*, *118*, 190–205. https://doi.org/10.1002/jgre.20045

Neumann, G. A., Zuber, M. T., Wieczorek, M. A., Head, J. W., Baker, D. M. H., Solomon, S. C., Smith, D. E., et al. (2015). Lunar impact basins revealed by Gravity Recovery and Interior Laboratory measurements. *Science Advances*, *1*(9), e1500852. https://doi.org/10.1126/sciadv.1500852

Pierazzo, E., Vickery, A. M., & Melosh, H. J. (1997). A reevaluation of impact melt production. *Icarus*, *127*(2), 408–423. https://doi.org/10.1006/icar.1997.5713

Potter, R. W. K. (2015). Investigating the onset of multi-ring impact basin formation. *Icarus*, *261*(C), 91–99. https://doi.org/10.1016/j.icarus.2015.08.009

Potter, R. W. K., Kring, D. A., Collins, G. S., Kiefer, W. S., & McGovern, P. J. (2012). Estimating transient crater size using the crustal annular bulge: Insights from numerical modeling of lunar basin-scale impacts. *Geophysical Research Letters*, *39*, L18203. https://doi.org/10.1029/2012GL052981

Potter, R. W. K., Kring, D. A., Collins, G. S., Kiefer, W. S., & McGovern, P. J. (2013). Numerical modeling of the formation and structure of the Orientale impact basin. *Journal of Geophysical Research: Planets*, *118*, 963–979. https://doi.org/10.1002/jgre.20080

Senft, L. E., & Stewart, S. T. (2009). Dynamic fault weakening and the formation of large impact craters. *Earth and Planetary Science Letters*, *287*(3–4), 471–482. https://doi.org/10.1016/j.epsl.2009.08.033

Spudis, P. D., Reisse, R. A., & Gillis, J. J. (1994). Ancient multiring basins on the Moon revealed by Clementine Laser Altimetry. *Science*, *266*(5192), 1848–1851. https://doi.org/10.1126/science.266.5192.1848

Wieczorek, M. A., Neumann, G. A., Nimmo, F., Kiefer, W. S., Taylor, G. J., Melosh, H. J., et al. (2013). The crust of the Moon as seen by GRAIL. *Science*, *339*(6120), 671–675. https://doi.org/10.1126/science.1231530

Wilhelms, D. E. (1987). The geologic history of the Moon. U.S. Geological Survey Prof. Paper 1348 (U.S. Gov. Printing Office).

Wünnemann, K., Collins, G. S., & Melosh, H. J. (2006). A strain-based porosity model for use in hydrocode simulations of impacts and implications for transient crater growth in porous targets. *Icarus*, *180*(2), 514–527. https://doi.org/10.1016/j.icarus.2005.10.013

Wünnemann, K., Collins, G. S., & Osinski, G. R. (2008). Numerical modelling of impact melt production in porous rocks. *Earth and Planetary Science Letters*, *269*(3–4), 530–539. https://doi.org/10.1016/j.epsl.2008.03.007

Yue, Z., Johnson, B. C., Minton, D. A., Melosh, H. J., Di, K., Hu, W., & Liu, Y. (2013). Projectile remnants in central peaks of lunar impact craters. *Nature Geoscience*, *6*(6), 435–437. https://doi.org/10.1038/ngeo1828

Zuber, M. T., Smith, D. E., Neumann, G. A., Goossens, S., Andrews-Hanna, J. C., Head, J. W., et al. (2016). Gravity field of the Orientale basin from the Gravity Recovery and Interior Laboratory mission. *Science*, *354*(6311), 438–441. https://doi.org/10.1126/science.aag0519